Electrocatalytic Nitrous Oxide Reduction Reaction at Sn-modified Pd–Pt Single Crystalline Electrodes in Acidic Media

Masaru Kato,[1,2*] Jinhang Zheng,[2] Yang Deng,[3,+] Fumie Saito,[2] Yuki Unuma,[2] Sayuki Oka,[2,++] Kazuhisa Tamura,[4] Ichizo Yagi[1,2*]

[1]Faculty of Environmental Earth Science, Hokkaido University, N10W5, Kita-ku, Sapporo 060-0810, Japan
[2]Graduate School of Environmental Science, Hokkaido University, N10W5, Kita-ku, Sapporo 060-0810, Japan
[3]Department of Environmental Engineering, Peking University, The Key Laboratory of Water and Sediment Sciences, Ministry of Education, Beijing 100871, China
[4]Materials Sciences Research Center, Japan Atomic Energy Agency, Koto 1-1-1, Sayo, Hyogo 679-5148, Japan

*Corresponding authors:
masaru.kato@ees.hokudai.ac.jp (MK), iyagi@ees.hokudai.ac.jp (IY)

+Present address: Department of Chemistry, University of North Dakota, Grand Forks, North Dakota 58202, United States
++Present address: Research Institute for Electronic Science, Hokkaido University, N21W10, Kita-ku, Sapporo 001-0021, Japan

Keywords. Nitrous oxide reduction reaction, single crystalline electrodes, *in situ* X-ray crystal truncation rod measurements, Sn modification, Pd-Pt(100), greenhouse gas removal, global warming mitigation, stratospheric ozone protection

Abstract

Nitrous oxide (N_2O) is a greenhouse gas and an ozone-depleting gas. Electrocatalytic N_2O reduction reaction (N_2ORR) is known to be catalyzed at noble metal electrodes such as Pd and Pt, and the surface modification of such noble metals with Sn is known to increase the N_2ORR in acidic media. However, the role of Sn at the surface remains unclear. In this work, N_2ORR activity was investigated for single crystalline Pt, Pd and Pd-Pt electrodes with the (111) or (100) plane in the presence and absence of Sn at the electrode surface in acidic media. *In situ* X-ray crystal truncation rod (CTR) measurements of Sn-modified Pt(111) and Pd(111) electrodes revealed the presence of metallic Sn and SnO, respectively, at their surfaces. The surface Sn modification enhances the N_2ORR activity for Pd-Pt(100) or Pd(100) electrodes but not for the Pt(111), Pd-Pt(111) or Pt(100) electrodes. The Sn-modified 15 at. % Pd-Pt(100) electrode shows higher N_2ORR activity than Sn-modified Pd(100) or Pt(100) electrodes, indicating that the co-presence of Pd and Pt at the (100) surface with Sn is important to maximize the N_2ORR activity. Density functional theory (DFT) calculations revealed that the N_2ORR activity of the Sn/Pd-Pt(100) electrode can be attributed to (1) the strong N_2O adsorption capacity of the (100) surface, (2) the reduction of H poisoning by Pd-Pt alloying, and (3) the activation of N_2O molecules by Sn modification. Our model studies using atomically defined single crystalline electrodes will enable researchers to design and develop practical N_2ORR electrocatalysts from the surface engineering point of view and then contribute to global warming mitigation and stratospheric ozone protection through N_2O removal.

1. Introduction

Nitrous oxide (N_2O) is a greenhouse gas nearly 300 times more potent than CO_2 and an ozone-depleting gas.[1-3] N_2O is increasing in the atmosphere by about one ppb per year. N_2O can be mainly produced from agriculture sectors and natural soils via a denitrification process, where nitrate (NO_3^-) can be reduced sequentially to dinitrogen (N_2) via N_2O. To protect the climate and the ozone layer, on-site N_2O removal techniques are highly desirable to contribute to sustainable development goals.

Electrocatalytic N_2O reduction reaction (N_2ORR) is an ideal option to remove N_2O ($N_2O + 2H^+ + 2e^- \rightarrow N_2 + H_2O$, E^o = 1.77 V vs. SHE): it can be driven by electrocatalysts at ambient conditions of room temperature and atmospheric pressure with low energy consumption using no external reducing agent.[3] At such mild conditions, N_2O decomposition has not been achieved for thermal or catalytic (direct catalytic decomposition or selective catalytic reduction).[3-4] As electrocatalysts, monometallic N_2ORR electrocatalysts have been studied for polycrystalline[5-7] and single crystalline electrodes.[8-10] In the monometallic electrodes, Pd is known to show high faradaic efficiency (almost 100%) to N_2 for the N_2ORR with relatively low overpotential.[3,5-7,11-12] As Pd alloy electrocatalysts for the N_2ORR, a Pd/Cu film,[13] carbon-supported Au@Pd core@shell nanoparticles,[14] fluorine-doped tin oxide (FTO)-supported Pt-Pd nanoparticles,[15] and carbon-supported PtPdSn nanoparticles[16] have been reported. In the case of Pt-Pd-Sn nanoparticles, the interface between Sn and Pt-Pd serves as the active site because much higher electrocatalytic N_2ORR activity with the contact with Sn specie was achieved. Although the role of Sn in the enhancement for the N_2ORR remains unclear, Sn species at the interface of the noble metal are believed to play important roles in N_2O adsorption and/or underpotentially deposited hydrogen (H_{upd}) because the N_2O adsorption to the metal surface is weak and H_{upd} hinders the N_2ORR on the Pd electrode.[8,17-18] The surface Sn modification has also been known to enhance other electrocatalytic reduction reactions such as the nitrate reduction reaction,[19-26] CO_2 reduction reaction,[27-29] oxygen reduction reaction,[30-31] and furfural reduction reactions.[32-33] These studies encouraged us to systematically study electrocatalytic activity of model Pd-Pt electrodes:[25-26,34] single crystalline Pd-Pt electrodes modified and unmodified Sn species for the N_2ORR.

In this work, we prepared single crystalline Pd-Pt(111) and Pd-Pt(100) electrodes with different atomic ratios. These single crystalline electrodes were unmodified or modified with Sn species and then studied their electrocatalytic N_2ORR activity in acidic media.

Systematic studies using single crystalline alloy electrodes enabled us to understand the effect of the surface atomic arrangement, composition and tin-modification on the N_2ORR activity. Density functional theory (DFT) calculations of Sn-modified Pd-Pt(100) electrodes revealed the role of the surface Sn in the N_2O adsorption and activation at the Pd-Pt(100) electrode.

2. Materials and Methods

2.1. Materials.

Sulfuric acid (95.0%) and nitric acid (95.0%) from Junsei Chemical were used to prepare mixed acid solutions for cleaning glassware. Sulfuric acid (99.999%) and perchloric acid (70%, purity: 99.999%) from Sigma-Aldrich were used for electrochemical measurements. Acetone and $SnCl_2 \cdot 2H_2O$ (97.0%) were purchased from Fujifilm Wako Pure Chemical and Kanto Chemical, respectively. Gas cylinders of Ar (99.9995%) and N_2O (99.99%) were commercially available from Air Water Hokkaido. Wires of platinum (99.99%, 0.8 mm in diameter) and palladium (99.99%, 0.8 and 0.5 mm in diameter) were purchased from Tanaka Kikinzoku Kogyo and Furuuchi Chemical, respectively. Pt(111) and Pd(111) disks (ϕ10 mm × 5 mm t) for surface X-ray scattering measurements were purchased from Surface Preparation Laboratory and MaTeck GmbH, respectively.

2.2. Electrode preparation.

Single crystal electrodes were prepared based on the preparation procedure previously reported.[24-26]

Single crystalline beads of Pt or Pd were obtained at the end of the corresponding metal wire in methane-oxygen flame. For the preparation of Pd-Pt single crystalline beads (5 or 15 at. % of Pd), Pd was added into the Pt single crystalline bead in methane-oxygen flame. The single crystalline beads were oriented using the reflection of the He–Ne laser beam from a (111) or (100) facet on the single crystalline bead, fixed in a poly(methyl methacrylate) resin (Technovit 4004, Heraeus Kulzer), cut in the direction of the facet, and then polished with diamond slurries to be mirror-finished. The polished single crystalline electrode with the resin was kept in dichloromethane overnight to remove the resin, and then ultrasonicated in acetone and Milli-Q water for 15 min each. The polished single crystalline electrode was annealed in methane-oxygen flame at about 1200 ºC for 4 h. The heating temperature was monitored by a radiation thermometer during annealing the electrode.

2.3. Electrochemical measurements.

Before electrochemical measurements, the glassware was kept in mixed acid (H_2SO_4:HNO_3 = 1:1, *v*/*v*) overnight to remove organic contaminants. After that, the glassware was kept in boiling Milli-Q water for 30 minutes and then rinsed with Milli-Q water. This cleaning process was repeated at least three times.

Before electrochemical measurements, Pd-Pt single crystalline electrodes were annealed under H_2–Ar for 10 min. in the glass-tubing chamber that is placed in an induction coil of an induction heating system (EASY–HEAT model 0224, Ambrell), cooled for 1 min under H_2–Ar, and then quickly immersed in Milli-Q water to protect the electrode surface with a droplet of Milli-Q water from surface contamination. Pd single crystalline electrodes were annealed in the same way except for under Ar because of the hydrogen absorption property of Pd. The water-protected single crystalline electrode was transferred into the electrochemical cell.

To confirm the well-defined electrode surface, cyclic voltammograms (CVs) of the single crystalline electrodes were recorded in a 0.5 M H_2SO_4 aqueous solution under Ar. The electrolyte solution was purged with Ar for at least 30 min before use. During the electrochemical measurements, the polished electrode surface was touched on the electrolyte solution in the hanging meniscus configuration. CVs of Pt and Pd-Pt electrodes were recorded at a sweep rate of 50 mV s^{-1} in the potential range between 0.05 and 0.85 V vs. RHE. CVs of Pd electrodes were recorded at 20 mV s^{-1} in the potential range between 0.18 and 1.4 V vs. RHE. To use Pd electrodes for the further electrochemical measurements after recording CVs in the 0.5 M H_2SO_4 solution, the annealing for 2 h is needed to reproduce the clean electrode surface.

The Sn modification on the electrode surface was performed in a 0.1 M $HClO_4$ aqueous solution containing 0.1 mM $SnCl_2$ for 1 to 20 s. The Sn coverage on the surface can be controlled by changing the immersion time to some extent. The Sn-modified electrode was rinsed in Ar-saturated Milli-Q water and then transferred into the electrochemical cell of the 0.5 M H_2SO_4 solution under Ar. To determine the surface coverage with Sn, CVs were recorded at 50 mV s^{-1} for ten cycles. CVs of tin-modified and unmodified electrodes in the underpotentially deposited hydrogen, H_{upd}, desorption region (≤0.5 V vs. RHE) allows us to determine the surface coverage with Sn based on the charges of H_{upd}, $\theta_{Sn}(H_{upd})$, using the following equation:

$$\theta_{Sn} = (Q_H^0 - Q_H) / Q_H^0,$$

where Q_H^0 and Q_H indicate the Faradaic charges corresponding to the desorption of H_{upd} before and after the tin modification, respectively.[24-26] Based on the CV in the 10th cycle, the surface coverage with Sn was determined.

To understand the electrocatalytic activity for the N_2ORR, CVs of electrodes were recorded in a 0.1 M $HClO_4$ aqueous solution under Ar as the background measurement and then under N_2O. CVs were recorded with five cycles at 10 mV s^{-1} in the potential range between 0.05 and 0.75 V vs. RHE, starting from 0.75 V vs. RHE. The electrolyte solution was purged with Ar or N_2O for at least 30 min before electrochemical measurements.

2.4. Auger electron spectroscopy (AES).

Before AES measurements, the electrode was cleaned under ultrasonication in acetone and Milli-Q water for 20 min each and then annealed in methane-oxygen flame at about 1200 ºC for 2 h. AES data were recorded using an Auger electron spectrometer (JAMP-9500F) under electron beam at 10 keV and 10 nA. Pd:Pt ratios of the prepared Pd-Pt single crystalline electrodes were determined from ratios of the differential intensity at 330 eV for Pd and 1967 eV for Pt.

2.5. *In situ* surface X-ray scattering (SXS).

SXS measurements were performed at the BL22XU station in SPring-8. Pt(111) and Pd(111) disk electrodes with 10 mm in diameter were used. The electrode was annealed in hydrogen flame for 1–2 min at about 1200ºC and then cooled under Ar for 10 min. The electrode surface was confirmed by recording CVs in a 0.5 M H_2SO_4 aqueous solution with hanging meniscus configuration. The electrode was modified with Sn at the surface in the same way mentioned above, and then fixed to the electrode holder in the home-made thin layer spectroelectrochemical cell,[35-36] made of Kel-F with the Pt wire counter and no-leak Ag|AgCl reference electrodes. A 6 μm-thick Myler film was used as the window of the spectroelectrochemical cell and the electrolyte solution was introduced in the cell chamber. The electrode potential was controlled by a potentiostat (Hokuto Denko, HAL3001A). The spectroelectrochemical cell was set on κ-type X-ray diffractometer installed in the undulator beamline BL22XU. Incident X-ray energies at 11.27 keV (wavelength: 1.09974 Å) and 11.29 keV (wavelength: 1.09828 Å) were used for SXS measurements at Pt(111) and Pd(111), respectively, to avoid any fluorescence from Pt and Pd electrodes. The coordinate system was hexagonal. The *a*- and *b*-axes were parallel to the electrode surface, while the *c*-axis was normal to the electrode surface. X-ray crystal

truncation rod (CTR) profiles of the reflectance along the (00) rod for the Sn-modified Pt(111) or Pd(111) electrodes were recorded in 0.1 M $HClO_4$ and 0.05 M H_2SO_4 aqueous solutions at 0.18 V vs. RHE under N_2, respectively.

2.6. Theoretical calculations

The initial structure model of the Pt crystal[37] is available for open access on the American Mineralogist Crystal Structure Database website.[38] The molecular structure was constructed and optimized using BURAI 1.3 software[39] based on the Quantum ESPRESSO framework.[40]

For the crystal surfaces, the (100) and (111) surface was modeled using a 2 × 2 cell configuration with 4 layers in total, where the bottom 2 layers were fixed. The ultrasoft Vanderbilt pseudopotential method with the Perdew–Burke–Ernzerhof (PBE) exchange-correlation functional was employed. A plane-wave cutoff energy of 400 eV was used, and the vacuum thickness in the calculations was set to 15 Å. The Brillouin zone was sampled using the Gamma point for the *k*-point grid, and atomic relaxations were carried out until the maximum force on any atom was reduced to less than 0.02 eV/Å. After optimization, the minimum energy of each structure was obtained, and the adsorption energy (E_{ads}) can be calculated using the following equation[41]:

$$E_{ads} = E_{mol+surf} - \left(E_{mol} + E_{surf}\right) \quad (1)$$

where E_{mol} and E_{surf} represent the energies (eV) of the isolated molecule and the surface, respectively, while $E_{mol+surf}$ denotes the total energy (eV) of the surface and molecule after adsorption.

The changes of projected density of states (PDOS) were calculated by the BURAI 1.3 software. The lowest unoccupied molecular orbital was determined at the position higher than the 0 eV vs E_f in the PDOS diagram.

3. Results and Discussion

3.1. Characterization of Pd-Pt(111), Pd-Pt(100) and Pd(100) electrodes.

Single crystalline electrodes for electrochemical measurements were prepared by the Clavilier method.[42-43] To obtain the target content of Pd (5 or 15 at. % of Pd) for Pd-Pt single crystalline electrodes, Pd was added into the Pt single crystalline bead in methane-oxygen flame.[25-26] The bead was cut in the direction of the (111) or (100) facets, polished and then annealed to obtain the single crystalline electrodes. To confirm the successful

preparation of the electrodes, CVs in a 0.5 M H_2SO_4 under Ar (**Figure 1**) and AES data (**Figures S1** and **S2** and **Table S1**) were recorded.

The Pt(111) electrode shows characteristic and symmetric waves in the potential range between 0.05 and 0.5 V vs. RHE in the CV recorded in the 0.5 M H_2SO_4 under Ar (**Figure 1a**):[42] hydrogen adsorption and desorption at 0.05-0.30 V vs. RHE; sulfate anion adsorption and desorption at 0.30-0.50 V; the phase transition of adsorbed sulfate anions on the Pt(111) surface as the characteristic spike at about 0.45 V vs. RHE. This spike decreases for Pd–Pt(111), suggesting that the long-range order of the Pt(111) terrace was lost and Pd atoms are randomly distributed not only the surface but also the bulk.[25,43] Instead of the spike at about 0.45 V for Pt(111), Pd-Pt(111) electrodes show sharp redox peaks at 0.3–0.35 V vs. RHE and the intensity increases with increasing the Pd content (**Figure 1a**). These peaks are associated with the adsorption and desorption of HSO_4^- /SO_4^{2-} on Pd(111) domains.[44-45] The characteristic voltametric profiles are similar to those for recently reported Pd-Pt(111) electrodes,[46] indicating the successful preparation of Pd-Pt(111) electrodes. AES data of the single crystalline electrodes labeled with 5 at. % Pd-Pt(111) and 15 at. % Pd-Pt(111) shows 5.1±0.8 and 16.9±2.2 at. % of Pd, respectively (**Table S1** and **Figure S2**), also indicating the successful doping of the target Pd content.

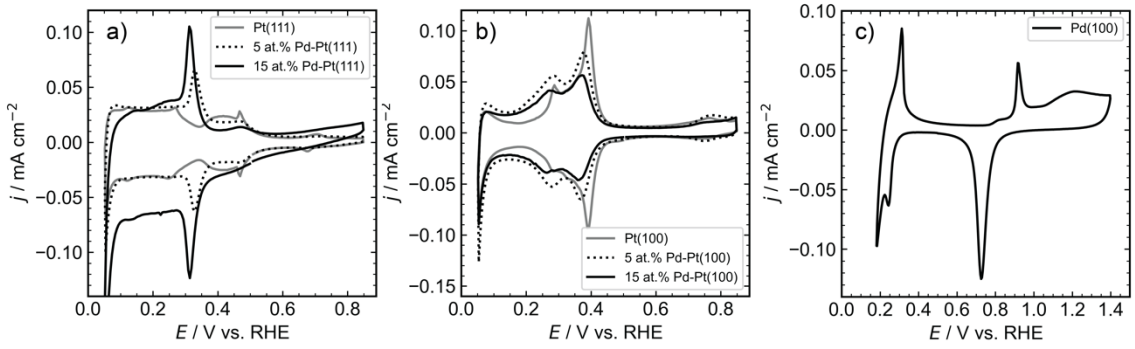

Figure 1. (a) CVs of Pt(111) (the solid line in gray), 5 at. % Pd-Pt(111) (the dotted line in black) and 15 at. % Pd-Pt(111) (the solid line in black). (b) CVs of Pt(100) (the solid trace in gray), 5 at. % Pd-Pt(100) (the dotted trace in black) and 15 at. % Pd-Pt(100) (the solid trace in black). These CVs were recorded at 50 mV s^{-1} in a 0.5 M H_2SO_4 aqueous solution at pH 0.45 under Ar. (c) A CV of Pd(100) recorded 20 mV s^{-1} in a 0.5 M H_2SO_4 aqueous solution at pH 0.45 under Ar.

The Pt(100) electrode shows characteristic peaks of hydrogen adsorption and desorption in the potential range from 0.2 to 0.4 V vs. RHE in the CV recorded in the 0.5

M H_2SO_4 aqueous solution under Ar (**Figure 1b**). The sharp peaks observed for Pt(100) at about 0.39 V vs. RHE are associated with extended (1x1)–Pt(100) long-range order.[47] The intensity of the Pt(100) terrace peak decreases and shifted to more negative potentials, which indicates the formation of the Pd-Pt(100) alloy single crystalline electrodes.[25-26,47] The characteristic voltametric profiles mentioned above are similar to those reported for Pd-Pt(100) electrodes,[46] confirming the successful preparation of Pd-Pt(100) electrodes. AES measurements of the electrodes labeled with 5 at. % Pd-Pt(100) and 15 at. % Pd-Pt(100) gave 6.0±1.0 and 14.7±3.5 at. % of Pd, respectively, confirming the successful preparation of the single crystalline electrodes (**Figure S2** and **Table S1**).

The CV of the Pd(100) electrode shows a sharp anodic peak at 0.35 V vs. RHE and a sharp cathodic peak at about 0.22 V vs. RHE (**Figure 1c**). These peaks are associated with the desorption and adsorption of HSO_4^-/SO_4^{2-} on the Pd(100) surface.[44] At ≤ 0.3 V vs. RHE, Pd(100) shows cathodic currents involving hydrogen absorption into palladium bulk overlapping the adsorption of sulfate anions. Characteristic anodic and cathodic peaks at about 0.90 and 0.73 V vs. RHE are assigned to be the formation and reduction of surface oxide, respectively.[26] The peak potential in the CV is in good agreement with those reported for the Pd(100) single crystalline electrode previously reported.[24-25,44] Thus, the Pd(100) single crystalline electrode was successfully prepared.

3.2. Sn surface modification

The surface of the single crystalline electrodes was modified with Sn by dipping the surface into a 0.1 M $HClO_4$ aqueous solution containing 0.1 mM $SnCl_2$.[25-26] The surface coverage of the electrode with Sn was determined based on the charge with the desorption of the H_{upd}, $\theta_{Sn}(H_{upd})$ (**Figures S3** and **S4**). The detection of Sn species in AES profiles also allows us to confirm the presence of Sn on single crystalline electrodes (**Figure S5**).

In situ X-ray crystal truncation rod (CTR) measurements and curve-fitting analysis of Sn/Pt(111) and Sn/Pd(111) (**Figure 2**) suggest the presence of metallic Sn on Pt(111) and SnO on Pd(111). The X-ray CTR measurement is a powerful technique to understand surface structures or coverages of adsorbed species on single crystalline electrodes.[48-51] Curve fitting analysis of the CTR profile of Sn/Pt(111) (**Figure 2a**) shows the best-fit result for a monolayer of metallic Sn with $\theta_{Sn}(CTR) = 0.32$ on the two Pt layers (**Table S2**). The $\theta_{Sn}(H_{upd})$ of the Sn/Pt(111) electrode was also determined to be about 0.65. The estimated coverage of the tin species by X-ray CTR measurements is lower than that

estimated by the electrochemical measurement. On the other hand, the curve-fitting analysis of CTR data of Sn/Pd(111) gave the best-fit result for a monolayer of SnO with θ_{Sn}(CTR) = 0.44 on the two Pd layers (**Figure 2b** and **Table S3**). These results indicate that oxidation state of tin species depends on the surface of the metal electrode used. The tin species tend to become higher oxidation states on Pd(111) than on Pt(111), which is in good agreement with X-ray photoelectron spectroscopy data previously reported.[25]

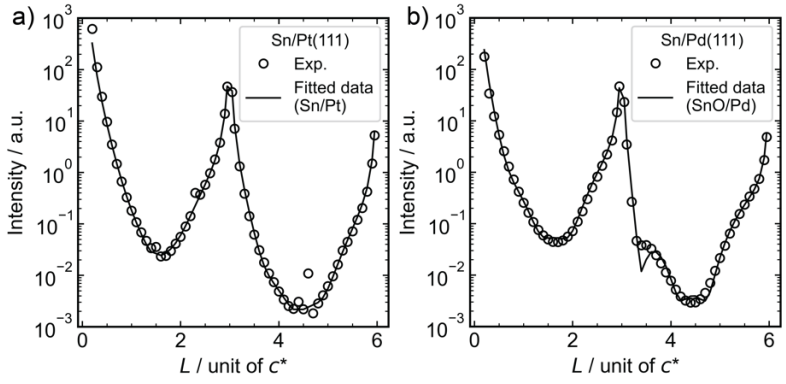

Figure 2. CTR profiles of the reflectance along the (00) rod (the circles) and the fitting results (the solid line) for (a) Sn/Pt(111) (the electrochemically estimated tin coverage is approximately 65%) at 0.18 V vs. RHE in a 0.1 M $HClO_4$ aqueous solution under N_2 and (b) Sn/Pd(111) (the electrochemically estimated tin coverage is approximately 40%) at 0.18 V vs. RHE in a 0.05 M H_2SO_4 aqueous solution under N_2. X-rays at 11.27 and 11.29 keV were used for Sn-modified Pt(111) and Pd(111) electrodes, respectively. For the fitting analysis, Sn^0 and $Sn^{II}O$ at the top layer were assumed for Sn-modified Pt(111) and Pd(111), respectively.

3.3. Electrocatalytic N_2ORR activity

Cyclic voltammograms (CVs) of single crystalline electrodes were recorded in a 0.1 M $HClO_4$ aqueous solution under Ar and N_2O to understand their electrocatalytic activity for the N_2ORR (**Figure 3**). Bare single crystalline Pt(111) and Pt(100) electrodes show cathodic currents under N_2O maximizing at around 0.4 V vs. RHE but almost no current under Ar (**Figure 3a** and **c**). These CVs under N_2O are the same as those of Pt(111) and Pt(100) previously reported.[8-9,18,52] Thus, the bare Pt(111) and Pt(100) electrodes have the electrocatalytic N_2ORR activity.

Although both of the bare Pt(111) and Pt(100) single crystalline electrodes show higher magnitudes of the N_2O reduction currents in the positive-going sweep than those

in the negative-going sweep, their CV shapes are different. The Pt(111) electrode shows the maximum cathodic current density for the N_2ORR centered at about 0.4 V vs. RHE in both of the positive- and negative-going sweeps (**Figure 3a**). This result indicates that the pzc of Pt(111) is about 0.4 V vs. RHE because it is proposed that N_2O serves as a chemical probe of the potential of zero charge (pzc): the maximum cathodic current for the N_2ORR occurs at a potential very close to or exactly at the pzc for Rh, Pd, Ir and Pt, where the N_2ORR involves competitive adsorption of N_2O with anions such as ClO_4^- and cations such as H^+ to the electrode surface.[8-9] In the case of the Pt(100) electrode, the positive-going sweep gives much higher current densities for the N_2ORR than the negative-going sweep (**Figure 3c**). The peak at about 0.25 V vs. RHE was assigned to the pzc on 1D ordered (100) sites whereas the peak at about 0.35 V vs. RHE was assigned to the pzc on Pt(100)-1x1 terrace sites.[9]

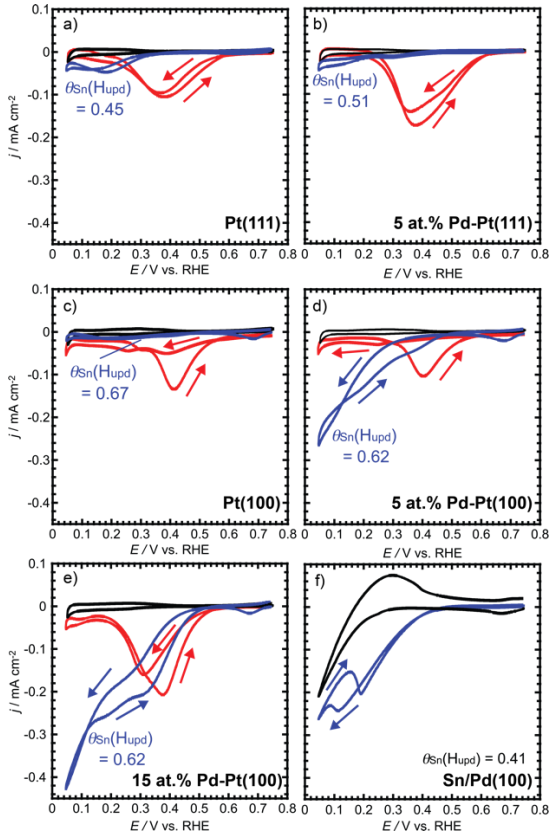

Figure 3. CVs of (a) Pt(111), (b) 5 at.% Pd-Pt(111), (c) Pt(100), (d) 5 at. % Pd-Pt(100) and (e) 15 at. % Pd-Pt(100) electrodes. The traces in black and red indicate the CVs of the electrodes with no Sn recorded under Ar and N_2O, respectively. The traces in blue show CVs of Sn-modified electrodes recorded under N_2O. (f) CVs of Sn/Pd(100) under Ar (in black) and N_2O (blue). All CVs were recorded at 10 mV s^{-1} in 0.1 M $HClO_4$

aqueous solutions. The Sn surface coverage based on the desorption of H_{upd} for each electrode is shown in each panel.

CVs of 5 at. % Pd-Pt(111) and Pd-Pt(100) electrodes show the similar cathodic currents under N_2O to those of the bare Pt(111) and Pt(100) electrodes, respectively (**Figure 3b** and **d**), indicating that these single crystalline alloy electrodes also have the electrocatalytic activity for the N_2ORR. There is no drastic difference in the peak-top potential for the N_2ORR between the non-doped and 5 at. % Pd-Pt electrodes, indicating that doping of 5 at. % of Pd into Pt(111) and Pt(100) electrodes has no almost impact on the N_2ORR activity as well as the pzc. We also observe no drastic difference in the magnitude of current densities for the N_2ORR between the non-doped and 5 at. % Pd-Pt electrodes even though Pd doping decreases current densities of the H_{upd} region (≤0.4 V vs. RHE) in CVs recorded in the 0.1 M $HClO_4$ aqueous solution under Ar (**Figure S6**). These results indicate that 5 at. % Pd doping into Pt electrodes is insufficient to significantly increase the N_2ORR activity and/or not only the H_{upd} but also other factors should be considered to understand the N_2ORR activity trend of Pd-Pt electrodes such as the adsorption of anions including perchlorate[53] and chloride, which can be produced by the decomposition of perchlorate anions.[8]

The surface modification of Sn increased the N_2ORR activity for 5 at. % Pd-Pt(100) whereas it almost completely suppressed the N_2ORR activity for Pt(111), 5 at. % Pd-Pt(111) or Pt(100) electrodes (**Figure 3a-d**). The Sn-modified 5 at. % Pd-Pt(100) electrode shows cathodic currents at ≤0.48 V vs. RHE. Although the onset potential of Sn-modified 5 at. % Pd-Pt(100) for the N_2ORR is shifted to more negative potentials than that of unmodified one, the cathodic current densities of Sn-modified 5 at. % Pd-Pt(100) reaches about –0.27 mA cm^{-2} at 0.05 V vs. RHE for the N_2ORR (**Figure 3d**). This current density is approximately three times higher than that of the unmodified electrode (about –0.1 mA cm^{-2} at 0.42 V vs. RHE). Note that the current densities of Sn-modified 5 at.% Pd-Pt(100) electrodes for the N_2ORR depends on the Sn surface coverage (**Figure S7**). It seems that the optimal $\theta_{Sn}(H_{upd})$ is around 0.6.

The Sn-modified 15 at. % Pd-Pt(100) electrode shows the highest N_2ORR activity in this work: its current density reaches about –0.43 mA cm^{-2} at 0.05 V vs. RHE for under N_2O (**Figure 3e**). These results indicate that the Sn modification at the electrode surface is effective to improve the N_2ORR activity for Pd-Pt alloy electrodes with the (100)

surface. The activity trend of the Sn-modified Pd-Pt alloy single crystalline electrodes at the (100) surface for the N_2ORR was determined as follows: Sn/Pt(100) < Sn/5 at. % Pd-Pt(100) < Sn/15 at. % Pd-Pt(100). The combination of Pd-Pt alloy formation and the (100) surface is important to maximize the N_2ORR activity in the 0.1 M $HClO_4$ aqueous solution because a CV of a Sn-modified Pd(100) electrode (**Figure 3f**) tends to show lower cathodic current densities than that of the Sn-modified 15 at. % Pd-Pt(100) electrode. The possible main product for the N_2ORR using Sn-modified Pd-Pt electrodes is N_2 rather than ammonia or hydroxylamine: Sn-modified Pd(100) and Pd-Pt(100) electrodes produced N_2 for the NO_3^- reduction reaction whereas Sn-modified Pt(100) electrodes did not produce N_2, confirmed by differential electrochemical mass spectrometry.[26] Recent studies on carbon-supported PtPdSn nanoparticles for the N_2ORR, which show almost 100% Faradaic efficiency to N_2 for the N_2ORR at ≥0.06 V vs. RHE, also suggesting that N_2 is the possible main product.[16] Note that the bare Pd(100) electrode also shows the N_2ORR activity (**Figure S8**). However, we have some issues with obtaining reproducible data. One of the main reasons possibly comes from the hydrogen absorption into pure Pd.

3.4. DFT calculations on the adsorption energy of N_2O

It is widely accepted that the N_2ORR on the electrode surface involves three key steps: N_2O adsorption, N_2O activation, and N_2O decomposition.[14] These steps are shown in the following equations:

$$N_2O \rightarrow *N_2O \quad (2)$$

$$*N_2O + e^- \rightarrow *N_2O^- \quad (3)$$

$$*N_2O^- + 2H^+ + e^- \rightarrow N_2 + H_2O \quad (4)$$

where * indicates the adsorption species. The N_2O adsorption step (Eq. 2) is generally regarded as the rate-determining step.[54] Additionally, in aqueous solutions, N_2O adsorption often involves competition with H adsorption.[8-9,15-16] Therefore, we also investigated the adsorption of H on each electrode for DFT calculations. The adsorption configurations of N_2O and H on the eight electrode surfaces are shown in **Figure 4a**.

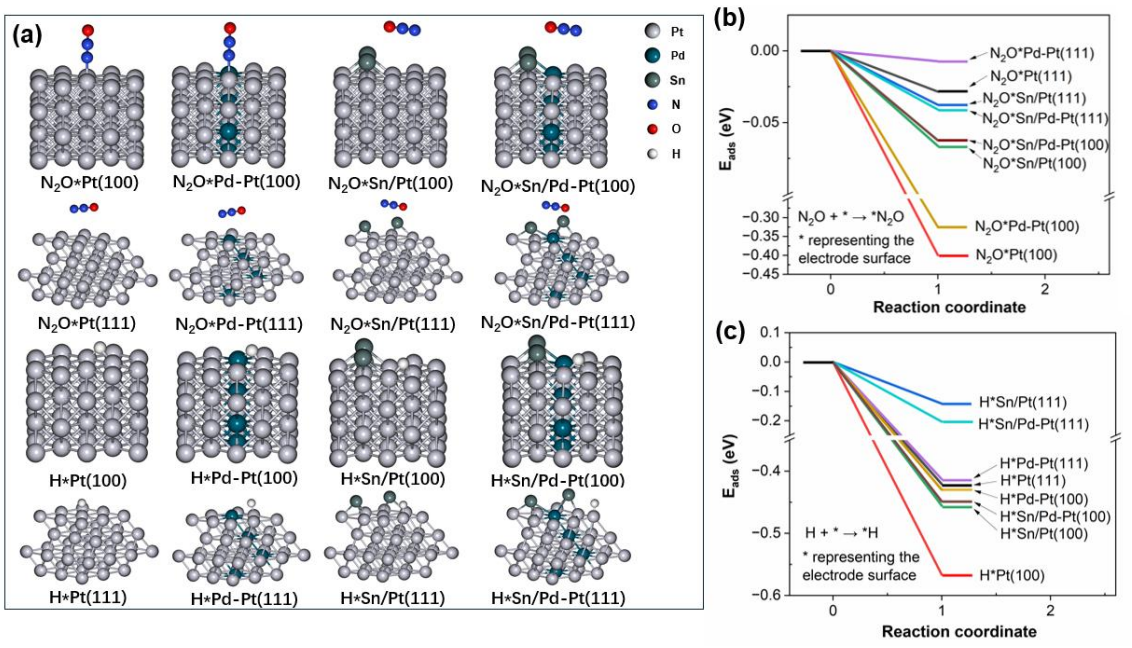

Figure 4 (a) The most stable adsorption configurations of N_2O and H on various crystal planes. (b) Adsorption energy of N_2O on various crystal planes. (c) Adsorption energy of H on various crystal planes. The adsorption energy calculation results are provided in **Tables S4** and **S5** in the SI.

For the N_2O adsorption on the (100) crystal planes, N_2O binds to the electrode surface through nitrogen atoms, forming a nearly vertical configuration. In contrast, on the (111) crystal planes, N_2O adopts a horizontal configuration relative to the electrode surface, which is consistent with previous reports.[14,55] Regarding H adsorption, after structural optimization, H is adsorbed at the bridging sites of the (100) crystal plane whereas H is primarily adsorbed at the top sites on the (111) crystal plane. These results align with previous studies.[56]

From the perspective of adsorption energy, N_2O adsorption on the (100) crystal plane is significantly stronger than on the (111) crystal plane with an adsorption energy ratio (**Figure 4b**), E_{ads}_Pt(100)/ E_{ads}_Pt(111), of 14.01 although N_2O can spontaneously bind to both the (111) and (100) crystal planes. These findings are similar to those reported for Pt(100) and Pt(111) electrodes.[55] In terms of H adsorption, the (100) crystal plane demonstrates a slightly stronger ability to adsorb H compared to the (111) crystal plane (**Figure 4c**), with an E_{ads}_Pt(100)/ E_{ads}_Pt(111) value of 1.35, closely matching the 1.29 previously reported.[56] Thus, the (100) crystal plane demonstrates substantially higher

activity in N_2O adsorption, leading to enhancing N_2ORR activity. In contrast, achieving efficient N_2ORR on the (111) crystal plane is challenging because of the competitive adsorption of H with N_2O. In the following discussion, we focus on the (100) crystal plane.

Pd-Pt alloying weakens the adsorption of both N_2O and H, compared with the Pt(100) crystal plane (**Figure 4b** and **4c**). The reductions in adsorption strength are 18.7% for N_2O and 24.1% for H, respectively, suggesting that Pd-Pt alloying has a more significant impact on weakening H adsorption. Consequently, Pd-Pt alloying enhances the competitiveness of N_2O adsorption by reducing H adsorption on the Pt(100) crystal plane, thereby mitigating the effects of H poisoning.

Sn modification leads to a reduction in the N_2O adsorption capacity on the (100) crystal plane (**Figure 4b**). Specifically, the thermodynamic energy barrier of N_2O adsorption on Pt(100) and Pd-Pt(100) increases by 0.33 eV and 0.26 eV, respectively, after Sn modification. As a result, the activity of Sn/Pd-Pt(100) suggests that Sn may play a crucial role in other aspects beyond N_2O adsorption, potentially having a significant impact on the N_2ORR activity of Sn/Pd-Pt(100).

We propose that Sn may play a role in facilitating electron transfer to adsorbed N_2O during the N_2ORR process. To test this hypothesis, we calculated the projected density of states (PDOS) for Sn on the Pd-Pt(100) electrode after N_2O adsorption (**Figure 5**). Upon adsorption of N_2O on the Pd-Pt(100) surface, the energy of the lowest unoccupied molecular orbital (LUMO) of the N_2O molecule is approximately 2.87 eV (**Figure 5a**). With the introduction of Sn, hybridization occurs between the Sn 5p orbital and the N 2p and O 2p orbitals of the N_2O molecule, leading to a reduction in the LUMO energy to approximately 2.78 eV (**Figure 5b**). Additionally, numerical analysis of the density of states indicates that Sn incorporation increases the LUMO state density of N_2O, potentially enhancing its ability to accept electrons during the reduction reaction. In summary, the combined effects of LUMO energy reduction and increased LUMO state density confirm that Sn can activate N_2O on the Pd-Pt(100) electrode and promote its decomposition into N_2 (Eqs. 3–4).

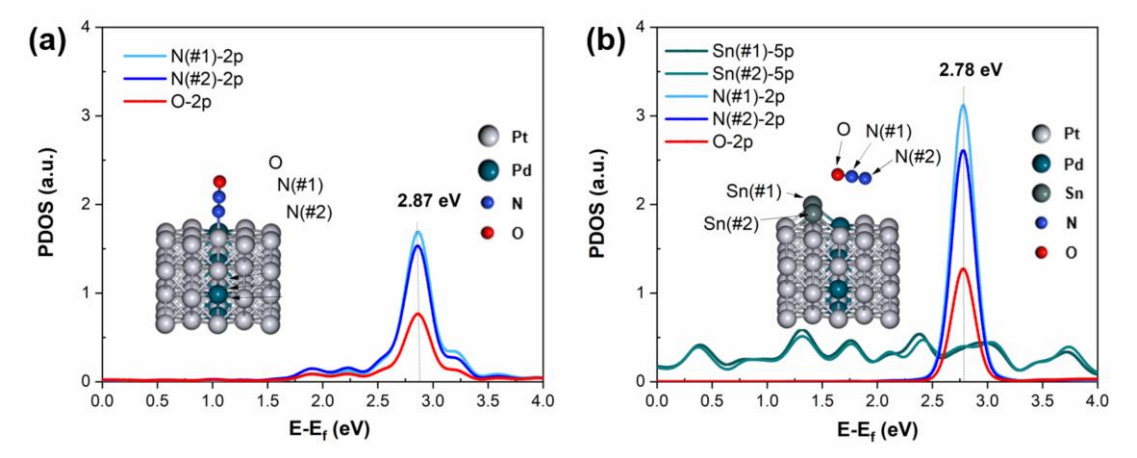

Figure 5 Effect of Sn modification on the energy level distribution of N_2O molecules after adsorption on the Pd-Pt(100) electrode. (a) PDOS diagram of Pd-Pt(100) without Sn modification; (b) PDOS diagram of Sn/Pd-Pt(100).

DFT calculations indicate that the N_2ORR activity of the Sn/Pd-Pt(100) electrode can be attributed to three key factors. Firstly, N_2O is strongly adsorbed to the (100) surface. Secondly, Pd-Pt alloying suppresses the H poisoning during the N_2O adsorption. Thirdly, the Sn modification activates the N-O bond in the N_2O molecule after the adsorption. These combined effects at the Pd-Pt(100) surface with the Sn adatom are responsible for enhancing N_2ORR activity on the Sn/Pd-Pt(100) electrode.

4. Conclusions

The electrocatalytic N_2ORR activity of Sn-modified Pd-Pt(111) and Pd-Pt(100) electrodes was studied in acidic media. The AES and *in situ* X-ray CTR measurements show the presence of Sn species even under electrochemical conditions: metallic Sn and SnO are present on the Pt(111) and Pd(111) surfaces, respectively. The surface Sn modification is effective on the enhancement of the electrocatalytic N_2ORR activity particularly for Pd-Pt(100) electrodes. The activity trend for the tin-modified electrodes was determined as follows: 15 at.% Pd-Pt(100) > Pd(100) > 5 at.% Pd-Pt(100) >> Pt(100). These results indicate that the interface of Pd-Pt(100) with the Sn species is crucial to efficiently catalyze the electrocatalytic N_2ORR. DFT calculations suggest that Pd-Pt alloying at the (100) surface is effective to drive the N_2O adsorption to the surface over the H_{upd} adsorption and the Sn modification helps the N–O bond cleavage at the surface. Our work demonstrates that surface engineering of electrocatalysts is crucial in N_2ORR

electrocatalysis, encouraging researchers to develop practical electrocatalysts with high N_2ORR activity and then to contribute both global warming mitigation and stratospheric ozone protection.

AUTHOR INFORMATION

Corresponding Authors

Emails: masaru.kato@ees.hokudai.ac.jp (MK); iyagi@ees.hokudai.ac.jp (IY)

ASSOCIATED CONTENT

Supporting Information.

The Supporting Information are available free of charge.

A SEM image of 15 at.% Pd-Pt(100), CVs of 5 at.% Pd-Pt(100) before and after the Sn modification, a differential AES profile of 15 at.% Pd-Pt(100) modified with Sn, CVs of Pd(100), atomic percentages of Pd for the alloy electrodes, and fitting parameters for X-ray CTR profiles. (PDF)

ACKNOWLEDGMENTS

The authors thank Takao Ohta (Graduate School of Engineering, Hokkaido University) for their technical support on electrochemical glassware. Auger electron spectroscopy was conducted at Laboratory of XPS analysis, Joint-use facilities, Hokkaido University. This work was supported by JSPS KAKENHI (Grant numbers: JP16K20882 and JP21K05124 to MK and JP19H02664 to IY), the Nanotechnology Platform program of the Ministry of Education, Culture, Sports, Science and Technology (MEXT) for Hokkaido University (JPMXP09A19HK0030 and JPMXP09A21HK0062) and "Advanced Research Infrastructure for Materials and Nanotechnology in Japan (ARIM)" of the MEXT (JPMXP1222HK0033) and the New Energy and Industrial Technology Development Organization (NEDO) (JPNP20003). The synchrotron radiation experiments were performed at the BL22XU of SPring-8 with the approval of the Japan Synchrotron Radiation Research Institute (JASRI) (Proposal Nos. 2021A3736, 2021B3736, 2022A3736, 2022B3736, and 2023A3736).

References

1. Tian, H.; Xu, R.; Canadell, J. G.; Thompson, R. L.; Winiwarter, W.; Suntharalingam, P.; Davidson, E. A.; Ciais, P.; Jackson, R. B.; Janssens-Maenhout, G.; Prather, M. J.; Regnier, P.; Pan, N.; Pan, S.; Peters, G. P.; Shi, H.; Tubiello, F. N.; Zaehle, S.; Zhou, F.; Arneth, A.; Battaglia, G.; Berthet, S.; Bopp, L.; Bouwman, A. F.; Buitenhuis, E. T.; Chang, J.; Chipperfield, M. P.; Dangal, S. R. S.; Dlugokencky, E.; Elkins, J. W.; Eyre, B. D.; Fu, B.; Hall, B.; Ito, A.; Joos, F.; Krummel, P. B.; Landolfi, A.; Laruelle, G. G.; Lauerwald, R.; Li, W.; Lienert, S.; Maavara, T.; MacLeod, M.; Millet, D. B.; Olin, S.; Patra, P. K.; Prinn, R. G.; Raymond, P. A.; Ruiz, D. J.; van der Werf, G. R.; Vuichard, N.; Wang, J.; Weiss, R. F.; Wells, K. C.; Wilson, C.; Yang, J.; Yao, Y. A comprehensive quantification of global nitrous oxide sources and sinks. *Nature* **2020**, *586*, 248-256. DOI: 10.1038/s41586-020-2780-0.

2. Ravishankara, A. R.; Daniel, J. S.; Portmann, R. W. Nitrous Oxide (N₂O): The Dominant Ozone-Depleting Substance Emitted in the 21st Century. *Science* **2009**, *326*, 123-125. DOI: 10.1126/science.1176985.

3. Wu, X.; Du, J.; Gao, Y.; Wang, H.; Zhang, C.; Zhang, R.; He, H.; Lu, G.; Wu, Z. Progress and challenges in nitrous oxide decomposition and valorization. *Chem. Soc. Rev.* **2024**, *53*, 8379-8423. DOI: 10.1039/D3CS00919J.

4. Galle, M.; Agar, D. W.; Watzenberger, O. Thermal N2O decomposition in regenerative heat exchanger reactors. *Chem. Eng. Sci.* **2001**, *56*, 1587-1595. DOI: 10.1016/S0009-2509(00)00386-9.

5. Kudo, A.; Mine, A. Electrocatalysis for N2O reduction on metal electrodes. *J. Electroanal. Chem.* **1996**, *408*, 267-269. DOI: 10.1016/0022-0728(96)04630-X.

6. Ko, B. H.; Hasa, B.; Shin, H.; Zhao, Y.; Jiao, F. Electrochemical Reduction of Gaseous Nitrogen Oxides on Transition Metals at Ambient Conditions. *J. Am. Chem. Soc.* **2022**, *144*, 1258-1266. DOI: 10.1021/jacs.1c10535.

7. Kudo, A.; Mine, A. Electrocatalytic reduction of nitrous oxide on metal and oxide electrodes in aqueous solution. *Appl. Surf. Sci.* **1997**, *121-122*, 538-542. DOI: 10.1016/S0169-4332(97)00362-0.

8. Ahmadi, A.; Bracey, E.; Wyn Evans, R.; Attard, G. Anion-surface interactions: Part II. Nitrous oxide reduction as a probe of anion adsorption on transition metal surfaces. *J. Electroanal. Chem.* **1993**, *350*, 297-316. DOI: 10.1016/0022-0728(93)80212-Z.

9. Attard, G. A.; Ahmadi, A. Anion—surface interactions Part 3. N2O reduction as a chemical probe of the local potential of zero total charge. *J. Electroanal. Chem.* **1995**, *389*, 175-190. DOI: 10.1016/0022-0728(95)03927-9.
10. Gómez, R.; Weaver, M. J. Reduction of Nitrous Oxide on Iridium Single-Crystal Electrodes. *Langmuir* **2002**, *18*, 4426-4432. DOI: 10.1021/la015700b.
11. Wang, B.; Li, X.-y. Electrocatalytic Properties of Nitrous Oxide and Its Voltammetric Detection at Palladium Electrodeposited on a Glassy Carbon Electrode. *Anal. Chem.* **1998**, *70*, 2181-2187. DOI: 10.1021/ac970601h.
12. Shibata, M.; Murase, K.; Furuya, N. Electroreduction of Nitrous Oxide to Nitrogen at Gas Diffusion Electrodes with Various Metal Catalysts. *Denki Kagaku oyobi Kogyo Butsuri Kagaku* **1997**, *65*, 1039-1043. DOI: 10.5796/kogyobutsurikagaku.65.1039.
13. Baek, S.; Kim, K.; Kwon, O. S.; Kim, H.; Han, J. W.; Kwon, O. J.; Kim, J. J. Pd–Cu alloy catalyst synthesized by citric acid-assisted galvanic displacement reaction for N2O reduction. *J. Appl. Electrochem.* **2020**, *50*, 395-405. DOI: 10.1007/s10800-019-01396-x.
14. Kim, K.; Byun, J.; Kim, H.; Lee, K.-S.; Lee, H. S.; Kim, J.; Hyeon, T.; Kim, J. J.; Han, J. W. Systematic Approach to Designing a Highly Efficient Core–Shell Electrocatalyst for N2O Reduction. *ACS Catal.* **2021**, *11*, 15089-15097. DOI: 10.1021/acscatal.1c03832.
15. Sarker, A. C.; Kato, M.; Yagi, I. Electrocatalytic nitrate and nitrous oxide reduction at interfaces between Pt-Pd nanoparticles and fluorine-doped tin oxide. *Electrochim. Acta* **2022**, *425*, 140628. DOI: 10.1016/j.electacta.2022.140628.
16. Sarker, A. C.; Kato, M.; Kawamura, M.; Watanabe, T.; Yagi, I. Selective electrocatalysis of the nitrous oxide reduction reaction to nitrogen on carbon-supported Pt–Pd–Sn nanoparticles. *Catal. Sci. Technol.* **2024**, *14*, 4137-4141. DOI: 10.1039/D4CY00664J.
17. Aziznia, A.; Bonakdarpour, A.; Gyenge, E. L.; Oloman, C. W. Electroreduction of nitrous oxide on platinum and palladium: Toward selective catalysts for methanol–nitrous oxide mixed-reactant fuel cells. *Electrochim. Acta* **2011**, *56*, 5238-5244. DOI: 10.1016/j.electacta.2011.03.023.
18. Ebert, H.; Parsons, R.; Ritzoulis, G.; VanderNoot, T. The reduction of nitrous oxide on platinum electrodes in acid solution. *J. Electroanal. Chem. Interf. Electrochem.* **1989**, *264*, 181-193. DOI: 10.1016/0022-0728(89)80156-1.
19. Li, F.; Zhang, W.; Zhang, P.; Gong, A.; Kexun, L. Strategies of selective electroreduction of aqueous nitrate to N2 in chloride-free system: A critical review. *Green*

Energy Environ. **2024**, *9*, 198-216. DOI: 10.1016/j.gee.2022.09.007.
20. Li, W.; Huang, C.-P. Nitrate reduction on bimetallic (Pd0.09Sn0.91) electrodes: Effects of calcination temperature, electrode support, and quenching. *Electrochim. Acta* **2024**, *504*, 144955. DOI: 10.1016/j.electacta.2024.144955.
21. Wang, Z.; Richards, D.; Singh, N. Recent discoveries in the reaction mechanism of heterogeneous electrocatalytic nitrate reduction. *Catal. Sci. Technol.* **2021**, *11*, 705-725. DOI: 10.1039/D0CY02025G.
22. Zeng, Y.; Priest, C.; Wang, G.; Wu, G. Restoring the Nitrogen Cycle by Electrochemical Reduction of Nitrate: Progress and Prospects. *Small Methods* **2020**, *4*, 2000672. DOI: 10.1002/smtd.202000672.
23. Yang, J.; Calle-Vallejo, F.; Duca, M.; Koper, M. T. M. Electrocatalytic Reduction of Nitrate on a Pt Electrode Modified by p-Block Metal Adatoms in Acid Solution. *ChemCatChem* **2013**, *5*, 1773-1783. DOI: 10.1002/cctc.201300075.
24. Deng, Y.; Kato, M.; Zheng, J.; Feng, C.; Yagi, I. The pH dependence of the electrocatalytic nitrate reduction by tin-modified palladium(100) electrodes: Effects of structures of tin species and protonation of nitrite. *Electrochim. Acta* **2023**, *470*, 143301. DOI: 10.1016/j.electacta.2023.143301.
25. Kato, M.; Okui, M.; Taguchi, S.; Yagi, I. Electrocatalytic nitrate reduction on well-defined surfaces of tin-modified platinum, palladium and platinum-palladium single crystalline electrodes in acidic and neutral media. *J. Electroanal. Chem.* **2017**, *800*, 46-53. DOI: 10.1016/j.jelechem.2017.01.020.
26. Kato, M.; Unuma, Y.; Okui, M.; Qu, Y.; Zheng, J.; Taguchi, S.; Kiguchi, F.; Torihata, M.; Gao, Y.; Hoshi, N.; Yagi, I. Electrocatalytic activity and volatile product selectivity for nitrate reduction at tin-modified Pt(100), Pd(100) and Pd–Pt(100) single crystal electrodes in acidic media. *Electrochim. Acta* **2021**, *398*, 139281. DOI: 10.1016/j.electacta.2021.139281.
27. Li, Q.; Fu, J.; Zhu, W.; Chen, Z.; Shen, B.; Wu, L.; Xi, Z.; Wang, T.; Lu, G.; Zhu, J.-j.; Sun, S. Tuning Sn-Catalysis for Electrochemical Reduction of CO2 to CO via the Core/Shell Cu/SnO2 Structure. *J. Am. Chem. Soc.* **2017**, *139*, 4290-4293. DOI: 10.1021/jacs.7b00261.
28. Sarfraz, S.; Garcia-Esparza, A. T.; Jedidi, A.; Cavallo, L.; Takanabe, K. Cu–Sn Bimetallic Catalyst for Selective Aqueous Electroreduction of CO2 to CO. *ACS Catal.* **2016**, *6*, 2842-2851. DOI: 10.1021/acscatal.6b00269.

29. Yang, S.; Liu, Z.; An, H.; Arnouts, S.; de Ruiter, J.; Rollier, F.; Bals, S.; Altantzis, T.; Figueiredo, M. C.; Filot, I. A. W.; Hensen, E. J. M.; Weckhuysen, B. M.; van der Stam, W. Near-Unity Electrochemical CO2 to CO Conversion over Sn-Doped Copper Oxide Nanoparticles. *ACS Catal.* **2022**, *12*, 15146-15156. DOI: 10.1021/acscatal.2c04279.
30. Nagasawa, K.; Takao, S.; Nagamatsu, S.-i.; Samjeské, G.; Sekizawa, O.; Kaneko, T.; Higashi, K.; Yamamoto, T.; Uruga, T.; Iwasawa, Y. Surface-Regulated Nano-SnO2/Pt3Co/C Cathode Catalysts for Polymer Electrolyte Fuel Cells Fabricated by a Selective Electrochemical Sn Deposition Method. *J. Am. Chem. Soc.* **2015**, *137*, 12856-12864. DOI: 10.1021/jacs.5b04256.
31. Shen, X.; Nagai, T.; Yang, F.; Zhou, L. Q.; Pan, Y.; Yao, L.; Wu, D.; Liu, Y.-S.; Feng, J.; Guo, J.; Jia, H.; Peng, Z. Dual-Site Cascade Oxygen Reduction Mechanism on SnOx/Pt–Cu–Ni for Promoting Reaction Kinetics. *J. Am. Chem. Soc.* **2019**, *141*, 9463-9467. DOI: 10.1021/jacs.9b02286.
32. Guo, X.; Fu, H.; Yang, J.; Luo, L.; Zhou, H.; Xu, M.; Kong, X.; Shao, M.; Duan, H.; Li, Z. Promoting Electrocatalytic Hydrogenation of 5-Hydroxymethylfurfural over a Cooperative Ag/SnO2 Catalyst in a Wide Potential Window. *ACS Catal.* **2023**, *13*, 13528-13539. DOI: 10.1021/acscatal.3c03005.
33. Liu, X.; Sun, Y.; Ren, H.; Lin, Y.; Wu, M.; Li, Z. Cu–Sn Bimetallic Activated Carbon–Carbon Coupling for Efficient Furfural Electroreduction. *ACS Catal.* **2024**, *14*, 5817-5826. DOI: 10.1021/acscatal.3c06346.
34. Jordá-Faus, P.; Rizo, R.; Herrero, E.; Arán-Ais, R. M. Investigating Alloy-Induced Modifications in the Oxygen Reduction Reaction Mechanism on PtPd Single Crystals. *ACS Catal.* **2024**, *14*, 12833-12845. DOI: 10.1021/acscatal.4c03565.
35. Kondo, T.; Tamura, K.; Takahasi, M.; Mizuki, J.-i.; Uosaki, K. A novel spectroelectrochemical cell for in situ surface X-ray scattering measurements of single crystal disk electrodes. *Electrochim. Acta* **2002**, *47*, 3075-3080. DOI: 10.1016/S0013-4686(02)00226-8.
36. Ocko, B. M.; Wang, J. In *Synchrotron Techniques in Interfacial Electrochemistry*, Melendres, C. A., Tadjeddine, A., Eds. Springer Netherlands: Dordrecht, 1994; pp 127-155.
37. Wyckoff, R. W. G., *Crystal structures*. 2nd ed.; Interscience Publishers: 1963; Vol. 1.
38. Downs, R. T.; Hall-Wallace, M. The American Mineralogist crystal structure database. *American Mineralogist* **2003**, *88*, 247-250. DOI: 10.25504/FAIRsharing.6bfdfc.

39. BURAI 1.3 software. http://nisihara.wixsite.com/burai (accessed 2025-2-21).
40. Giannozzi, P.; Baroni, S.; Bonini, N.; Calandra, M.; Car, R.; Cavazzoni, C.; Ceresoli, D.; Chiarotti, G. L.; Cococcioni, M.; Dabo, I.; Dal Corso, A.; de Gironcoli, S.; Fabris, S.; Fratesi, G.; Gebauer, R.; Gerstmann, U.; Gougoussis, C.; Kokalj, A.; Lazzeri, M.; Martin-Samos, L.; Marzari, N.; Mauri, F.; Mazzarello, R.; Paolini, S.; Pasquarello, A.; Paulatto, L.; Sbraccia, C.; Scandolo, S.; Sclauzero, G.; Seitsonen, A. P.; Smogunov, A.; Umari, P.; Wentzcovitch, R. M. QUANTUM ESPRESSO: a modular and open-source software project for quantum simulations of materials. *J. Phys.: Cond. Mat.* **2009**, *21*, 395502. DOI: 10.1088/0953-8984/21/39/395502.
41. Orita, H.; Kubo, T.; Matsushima, T.; Kokalj, A. DFT Calculations of Adsorption and Decomposition of N2O on Rh(100). *J. Phys. Chem. C* **2010**, *114*, 21444-21449. DOI: 10.1021/jp106338t.
42. Clavilier, J. The role of anion on the electrochemical behaviour of a {111} platinum surface; an unusual splitting of the voltammogram in the hydrogen region. *J. Electroanal. Chem. Interf. Electrochem.* **1980**, *107*, 211-216. DOI: 10.1016/S0022-0728(79)80023-6.
43. Watson, D. J.; Attard, G. A. The electro-oxidation of glucose using platinum–palladium bulk alloy single crystals. *Electrochim. Acta* **2001**, *46*, 3157-3161. DOI: 10.1016/S0013-4686(01)00607-7.
44. Hoshi, N.; Kagaya, K.; Hori, Y. Voltammograms of the single-crystal electrodes of palladium in aqueous sulfuric acid electrolyte: Pd(S)-[n(111)×(111)] and Pd(S)-[n(100)×(111)]. *J. Electroanal. Chem.* **2000**, *485*, 55-60. DOI: 10.1016/S0022-0728(00)00098-X.
45. Wan, L.-J.; Suzuki, T.; Sashikata, K.; Okada, J.; Inukai, J.; Itaya, K. In situ scanning tunneling microscopy of adsorbed sulfate on well-defined Pd(111) in sulfuric acid solution. *J. Electroanal. Chem.* **2000**, *484*, 189-193. DOI: 10.1016/S0022-0728(00)00082-6.
46. Melle, G.; Scholten, F.; Feliu, J. M.; Herrero, E.; Cuenya, B. R.; Arán-Ais, R. M. Elucidating interfacial parameters of platinum–palladium bulk alloy single crystals. *J. Mater. Chem. A* **2024**, *12*, 15321-15333. DOI: 10.1039/D4TA01771D.
47. Watson, D. J.; Attard, G. A. Surface segregation and reconstructive behaviour of the (100) and (110) surfaces of platinum–palladium bulk alloy single crystals: a voltammetric and LEED/AES study. *Surf. Sci.* **2002**, *515*, 87-93. DOI: 10.1016/S0039-6028(02)01811-3.

48. Yang, Y.; Peltier, C. R.; Zeng, R.; Schimmenti, R.; Li, Q.; Huang, X.; Yan, Z.; Potsi, G.; Selhorst, R.; Lu, X.; Xu, W.; Tader, M.; Soudackov, A. V.; Zhang, H.; Krumov, M.; Murray, E.; Xu, P.; Hitt, J.; Xu, L.; Ko, H.-Y.; Ernst, B. G.; Bundschu, C.; Luo, A.; Markovich, D.; Hu, M.; He, C.; Wang, H.; Fang, J.; DiStasio, R. A., Jr.; Kourkoutis, L. F.; Singer, A.; Noonan, K. J. T.; Xiao, L.; Zhuang, L.; Pivovar, B. S.; Zelenay, P.; Herrero, E.; Feliu, J. M.; Suntivich, J.; Giannelis, E. P.; Hammes-Schiffer, S.; Arias, T.; Mavrikakis, M.; Mallouk, T. E.; Brock, J. D.; Muller, D. A.; DiSalvo, F. J.; Coates, G. W.; Abruña, H. D. Electrocatalysis in Alkaline Media and Alkaline Membrane-Based Energy Technologies. *Chem. Rev.* **2022**, *122*, 6117-6321. DOI: 10.1021/acs.chemrev.1c00331.

49. Fuchs, T.; Drnec, J.; Calle-Vallejo, F.; Stubb, N.; Sandbeck, D. J. S.; Ruge, M.; Cherevko, S.; Harrington, D. A.; Magnussen, O. M. Structure dependency of the atomic-scale mechanisms of platinum electro-oxidation and dissolution. *Nat. Cat.* **2020**, *3*, 754-761. DOI: 10.1038/s41929-020-0497-y.

50. Fuchs, T.; Briega-Martos, V.; Drnec, J.; Stubb, N.; Martens, I.; Calle-Vallejo, F.; Harrington, D. A.; Cherevko, S.; Magnussen, O. M. Anodic and Cathodic Platinum Dissolution Processes Involve Different Oxide Species. *Angew. Chem. Int. Ed.* **2023**, *62*, e202304293. DOI: 10.1002/anie.202304293.

51. Tamura, K. Comparative Study of the Underpotential Deposition of Bi in an Aqueous Electrolyte and an Ionic Liquid. *J. Phys. Chem. C* **2023**, *127*, 22733-22739. DOI: 10.1021/acs.jpcc.3c05404.

52. Gutiérrez de Dios, F. J.; Gómez, R.; Feliu, J. M. Preparation and electrocatalytic activity of Rh adlayers on Pt(100) electrodes: reduction of nitrous oxide. *Electrochem. Commun.* **2001**, *3*, 659-664. DOI: 10.1016/S1388-2481(01)00243-0.

53. Chen, X.; Granda-Marulanda, L. P.; McCrum, I. T.; Koper, M. T. M. Adsorption processes on a Pd monolayer-modified Pt(111) electrode. *Chem. Sci.* **2020**, *11*, 1703-1713. DOI: 10.1039/C9SC05307G.

54. Rosca, V.; Duca, M.; de Groot, M. T.; Koper, M. T. M. Nitrogen Cycle Electrocatalysis. *Chem. Rev.* **2009**, *109*, 2209-2244. DOI: 10.1021/cr8003696.

55. Gonzalez, J. D.; Warner, M.; Haynes, B. S.; Montoya, A. N2O formation and dissociation during ammonia combustion: A combined DFT and experimental study. *Proceedings of the Combustion Institute* **2017**, *36*, 637-644. DOI: 10.1016/j.proci.2016.05.004.

56. Aguilera-Porta, N.; Calatayud, M.; Salzemann, C.; Petit, C. Understanding How in

Situ Generated Hydrogen Controls the Morphology of Platinum Nanoparticles. *J. Phys. Chem. C* **2014**, *118*, 9290-9298. DOI: 10.1021/jp502174b.

SYNOPSIS